

# Strange Vector Form Factors from Parity-Violating Electron Scattering

Kent Paschke<sup>1</sup>, Anthony Thomas<sup>2</sup>, Robert Michaels<sup>3</sup>, and David Armstrong<sup>4</sup>

<sup>1</sup> University of Virginia, Charlottesville, Virginia 22903, USA

<sup>2</sup> University of Adelaide, South Australia 5005, Australia

<sup>3</sup> Jefferson Lab, Newport News, Virginia 23606, USA

<sup>4</sup> College of William and Mary, Williamsburg, Virginia 23187, USA

**Abstract.** The simplest models might describe the nucleon as 3 light quarks, but this description would be incomplete without inclusion of the sea of glue and  $q\bar{q}$  pairs which binds it. Early indications of a particularly large contribution from strange quarks in this sea to the spin and mass of the nucleon motivated an experimental program examining the role of these strange quarks in the nucleon vector form factors. The strangeness form factors can be extracted from the well-studied electromagnetic structure of the nucleon using parity-violation in electron-nuclear scattering to isolate the effect of the weak interaction. With high luminosity and polarization, and a very stable beam due to its superconducting RF cavities, CEBAF at Jefferson Lab is a precision instrument uniquely well suited to the challenge of measurements of the small parity-violating asymmetries. The techniques and results of the two major Jefferson Lab experimental efforts in parity-violation studies, HAPPEX and G0, as well as efforts to describe the strange form factors in QCD, will be reviewed.

## 1. Introduction

The achievement which clearly identified Quantum Electrodynamics (QED) as the correct theory of the electromagnetic interaction was the quantitative explanation of the measurement of the Lamb shift in hydrogen. For the strong force we have Quantum Chromodynamics (QCD), a local gauge theory built on color, which has been verified with considerable precision in the high energy, “asymptotically free” regime. However, in the nonperturbative regime, where QCD is truly strong, it is still being tested, as our capacity for calculation using lattice QCD grows. By analogy with the Lamb shift in QED, a fundamental test of QCD in the nonperturbative regime is its capacity to accurately explain vacuum polarization. Since there are no strange valence quarks in the proton, the strangeness form factors of the nucleon present the ideal testing ground.

Historically, the enormous interest in the strangeness form factors arose from two things. The discovery of the EMC spin crisis, with its very small fraction of the proton spin carried by quarks, was widely interpreted in terms of a large negative fraction of the proton spin carried by strange quarks  $-\Delta s = -0.16 \pm 0.08$  [1]. At about the same time, analysis of the octet baryon masses in terms of SU(3) symmetry suggested values of the strangeness sigma commutator,  $\sigma_s = \langle p | m_s \bar{s}s | p \rangle$ , as large as 330 MeV [2]. Since  $\sigma_s = 330$  MeV represents a contribution to the nucleon mass of more than one third from a single sea quark flavor, this was an astonishing result. Both of these indications suggested a far greater role for the strange quark in proton structure

than had been anticipated before. Modern lattice estimates of the strange sigma commutator suggest a value almost an order of magnitude smaller [3]. In addition, it seems likely that SU(3) breaking leads to a considerably smaller value of  $\Delta s$  [4]. Nevertheless, in the late 1980's the older values were a powerful motivation for the experimental program.

In this environment, a number of authors estimated the strange quark charge radius and the strange magnetic moment of the proton in various models. Indeed, almost the entire arsenal of hadronic models have been brought to bear on the question of the strange form factors, including, but not limited to, vector meson dominance, the Skyrme model, kaon loops, the chiral quark model, dispersion relations, the NJL model, the quark-meson coupling model, the chiral bag model, heavy-baryon chiral perturbation theory, *etc.*; reviews of these are available elsewhere [5, 6]. Many reported large values. For example, Jaffe [7] found  $\langle r_s^2 \rangle = 0.16 \pm 0.06 \text{ fm}^2$  and  $\mu_s = -0.31 \pm 0.09 \mu_N$ , while Jaffe and Manohar observed [1] that until “such time as these experiments are perfected, the prediction of  $F_2^{(0)}$  remains an excellent goal for theorists who think they have understood the flavor structure of the proton.”

This excited theoretical discussion inspired novel experimental suggestions as to how one might actually measure these elusive quantities and it became clear that parity-violating electron scattering was the tool of choice [8, 9]. Thus began a rigorous and demanding program lasting more than 20 years, which as we report, has experimentally defined the strange electric and magnetic form factors of the proton. This program would not have been possible without the long term support of funding agencies and major laboratories, including MIT Bates, Mainz and, of course, Jefferson Lab.

Ignoring the tremendous technological and experimental challenges, the principle of the measurement of the strange vector form factors is simple. There are three vector operators whose matrix elements must be determined,  $\bar{q}\gamma^\mu q$  with  $q = u, d$  and  $s$ . Using charge symmetry, which is respected at better than 1% by the strong force, one obtains two constraints from the proton and neutron electromagnetic form factors. For the third constraint, the fact that the weak vector charges differ from the electromagnetic charges means that the measurement of parity-violating electron scattering from the proton is sufficient. Indeed, a measurement of the left-right asymmetry,  $A_{\text{LR}}$ , in the scattering of longitudinally polarized electrons from an unpolarized proton target yields the strange form factors through

$$A_{\text{LR}} = -\frac{G_F Q^2}{4\pi\alpha\sqrt{2}} \left\{ (1 - 4\sin^2\theta_W) - \frac{\epsilon G_E^p G_E^n + \tau G_M^p G_M^n}{\epsilon(G_E^p)^2 + \tau(G_M^p)^2} - \frac{\epsilon G_E^p G_E^s + \tau G_M^p G_M^s}{\epsilon(G_E^p)^2 + \tau(G_M^p)^2} - \frac{(1 - 4\sin^2\theta_W)\epsilon' G_M^p G_A^p}{\epsilon(G_E^p)^2 + \tau(G_M^p)^2} \right\}. \quad (1)$$

Here  $\tau = Q^2/4M_p^2$ ,  $\epsilon = \left(1 + 2(1 + \tau)\tan^2\frac{\theta}{2}\right)^{-1}$ , and  $\epsilon' = \sqrt{\tau(1 + \tau)(1 - \epsilon^2)}$ .  $G_E^s(Q^2)$  and  $G_M^s(Q^2)$  are the strange electric and strange magnetic form factors, respectively, and parameterize the strange quark contribution to the vector structure of the nucleon. Also appearing in this expression is the axial form factor  $G_A^p$ , which becomes significant at backward scattering angles where  $\epsilon'$  is larger. To lowest order, this form factor is the same as is measured in charged-current neutrino scattering. However, for electron scattering, large radiative corrections are expected to modify  $G_A^p$ . Decomposing  $G_A^p$  into isoscalar  $G_A^e(T = 0)$ , and  $G_A^e(T = 1)$  pieces, Zhu *et al.* [10] found, in a model-dependent analysis, that the radiative corrections for the isoscalar piece are small and under reasonable theoretical control, while the isovector part is large ( $\sim 30\%$ ) and less-well constrained theoretically. This latter term is interesting in its own right, as it includes the effective parity-violating coupling of the photon to the nucleon, the so-called “anapole” term [11], and, as we will describe, the parity-violating electron scattering program described here can also shed some light on this topic.

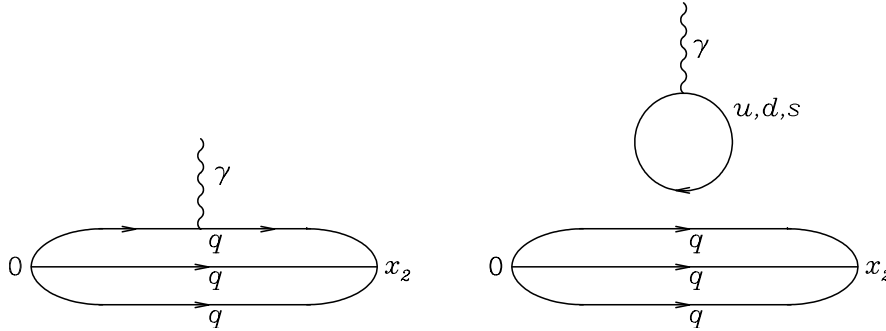


**Figure 1.** Diagrams illustrating the two topologically different insertions of the current within the framework of lattice QCD.

In this chapter, we first discuss the prediction of strange form factors from modern theory, focusing on lattice QCD. We then describe the experimental aspects of this program at Jefferson Lab. Then we present briefly the global analysis which yields the strange form factors, compare the extracted form factors with theory, and provide an outlook for the future.

## 2. Calculation of strange form factors within QCD

While the theoretical study of strange form factors within QCD cannot lay claim to two decades of effort, it is not so far off. Indeed, the initial studies of the electromagnetic form factors of the octet baryons began in the early 1990's, with work by Leinweber, Woloshyn and Draper [12]. It was these studies which gave direct information on the contribution to the baryon form factors from individual valence quarks that eventually led, some 14 years later, to remarkably accurate predictions [13, 14] of the strange quark form factors. The technique used in this work was indirect [15], so that for the strange magnetic moment it was necessary to combine lattice QCD calculations of the valence form factors, under the assumption of charge symmetry, with experimental information on the octet magnetic moments. This work required control of the extrapolation of the valence moments as a function of quark mass in both quenched and full QCD [16]. Only in the last two years (so again two decades from the first calculations) has it been possible to make a direct calculation in full QCD, with the Kentucky group reporting very accurate values of the strange magnetic moment of the proton in very good agreement with the earlier indirect calculations and with experiment.

### 2.1. Indirect method

As illustrated in Fig. 1, the three point function required to extract a magnetic moment in lattice QCD involves two topologically distinct processes. (Of course, in full QCD these diagrams incorporate an arbitrary number of gluons and quark loops.) The left-hand diagram illustrates the connected insertion of the current to one of the “valence” quarks of the baryon. In the right-hand diagram the external field couples to a quark loop. The latter process, where the loop involves an  $s$ -quark, is entirely responsible for the strange quark contribution to the nucleon form factor.

Under the assumption of charge symmetry [17], the magnetic moments of the octet baryons satisfy [15]:

$$\begin{aligned}
 p &= e_u u^p + e_d d^p + O_N ; \quad n = e_d u^p + e_u d^p + O_N , \\
 \Sigma^+ &= e_u u^\Sigma + e_s s^\Sigma + O_\Sigma ; \quad \Sigma^- = e_d u^\Sigma + e_s s^\Sigma + O_\Sigma , \\
 \Xi^0 &= e_s s^\Xi + e_u u^\Xi + O_\Xi ; \quad \Xi^- = e_s s^\Xi + e_d u^\Xi + O_\Xi .
 \end{aligned}$$

(2)

Here,  $p$  and  $\Xi^-$  are the physical magnetic moments of the proton and  $\Xi^-$ , and similarly for the other baryons. The valence  $u$ -quark sector magnetic moment in the proton, corresponding to the left hand side of Fig. 1, is denoted  $u^p$ . Charge symmetry has been used to replace the  $d$ -quark contribution in the neutron by  $u^p$ ,  $d$  in the  $\Sigma^-$  by  $u$  in the  $\Sigma^+$  ( $u^\Sigma$ ), and so on. The labels on quark magnetic moments allow for the environment sensitivity implicit in the three-point function. That is, the naive expectations of the constituent quark model, namely  $u^p/u^\Sigma = u^n/u^\Xi = 1$ , may not be satisfied. The total contribution from quark-loops,  $O_N$ , contains sea-quark-loop contributions (right hand side of Fig. 1) from  $u$ ,  $d$  and  $s$  quarks. By definition

$$O_N = \frac{2}{3} \ell G_M^u - \frac{1}{3} \ell G_M^d - \frac{1}{3} \ell G_M^s, \quad (3)$$

$$= \frac{\ell G_M^s}{3} \left( \frac{1 - \ell R_d^s}{\ell R_d^s} \right), \quad (4)$$

where the ratio of  $s$ - and  $d$ -quark loops,  $\ell R_d^s \equiv \ell G_M^s / \ell G_M^d$ , is expected to lie in the range (0,1). Note that, in deriving Eq. (4), we have used charge symmetry to set  $\ell G_M^u = \ell G_M^d$ . Since the chiral coefficients for the  $d$  and  $s$  loops in the right hand side of Fig. 1 are identical, the main difference comes from the mass of the  $K$  compared with that of the  $\pi$ .

With a little algebra,  $O_N$ , and hence  $G_M^s (\equiv \ell G_M^s)$ , may be isolated from Eqs. (2) and (4):

$$G_M^s = \left( \frac{\ell R_d^s}{1 - \ell R_d^s} \right) \left[ 2p + n - \frac{u^p}{u^\Sigma} (\Sigma^+ - \Sigma^-) \right], \quad (5)$$

$$G_M^s = \left( \frac{\ell R_d^s}{1 - \ell R_d^s} \right) \left[ p + 2n - \frac{u^n}{u^\Xi} (\Xi^0 - \Xi^-) \right]. \quad (6)$$

After incorporating the experimentally measured baryon moments [18] (in nuclear magnetons,  $\mu_N$ ), Eqs. (5) and (6) become:

$$G_M^s = \left( \frac{\ell R_d^s}{1 - \ell R_d^s} \right) \left[ 3.673 - \frac{u^p}{u^\Sigma} (3.618) \right], \quad (7)$$

$$G_M^s = \left( \frac{\ell R_d^s}{1 - \ell R_d^s} \right) \left[ -1.033 - \frac{u^n}{u^\Xi} (-0.599) \right]. \quad (8)$$

We stress that these expressions for  $G_M^s$  are exact consequences of QCD, under the assumption of charge symmetry.

Equating (7) and (8) provides a linear relationship between  $u^p/u^\Sigma$  and  $u^n/u^\Xi$  which must be satisfied within QCD under the assumption of charge symmetry. Clearly this linear relationship is inconsistent with the assumption of universality of the valence quark moments (*i.e.*, the point (1.0,1.0) does not lie on the empirical line). In addition, it is important from the point of view of reducing systematic errors that the linear relation involves only *ratios* of moments, which can be calculated more accurately than absolute values.

The actual lattice simulations gave the individual valence quark moments as a function of pion mass in quenched QCD. These were then fit using finite range regulated effective field theory on a finite volume, with coefficients for quenched QCD, which were then replaced by full QCD chiral corrections on an infinite volume. From this chiral extrapolation procedure, the ratios of the valence (connected)  $u$ -quark contributions,  $u^p/u^\Sigma$  and  $u^n/u^\Xi$  were calculated. The final results

$$\frac{u^p}{u^\Sigma} = 1.092 \pm 0.030 \quad \text{and} \quad \frac{u^n}{u^\Xi} = 1.254 \pm 0.124 \quad (9)$$

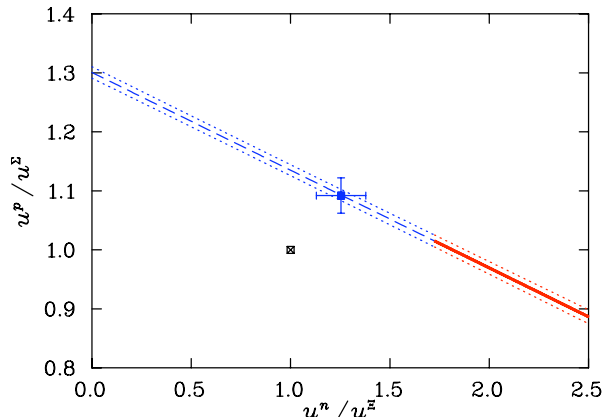


**Figure 2.** The constraint (dashed  $G_M^s(0) < 0$ , solid  $G_M^s(0) > 0$ ) on the ratios  $u^p/u^\Sigma$  and  $u^n/u^\Xi$  implied by charge symmetry and experimental moments. Experimental uncertainties are indicated by the dotted bounds. The assumption of environment-independent quark moments is indicated by the crossed square. The final result (chiral-corrected extrapolation of lattice results) is illustrated by the filled square, which does indeed lie on the charge symmetry line.

are plotted in Fig. 2. The precision of these results follows from the use of correlated ratios of moments which act to reduce uncertainties associated with the lattice spacing, the regulator mass and statistical fluctuations [19]. This result leaves no doubt that  $G_M^s$  is negative. The fact that this point lies exactly on the constraint curve is highly nontrivial, and provides a robust check of the validity of the analysis techniques.

While  $G_M^s$  was certainly negative, it remained to set the magnitude. This required an estimate of the strange to light sea-quark loop contributions,  ${}^\ell R_d^s$ . Earlier estimates of  ${}^\ell R_d^s$  had been based on the constituent quark model. A more reliable approach is to estimate the loops using the same successful model invoked to correct the quenched results to full QCD [16, 20]. Allowing the dipole mass parameter to vary between 0.6 and 1.0 GeV provides  ${}^\ell R_d^s = G_M^s/G_M^d = 0.139 \pm 0.042$ . A complete analysis of the errors associated with the determination of  $G_M^s$  using Eqs. (5), (6) and (9) is reported in Ref. [19]. The uncertainty is dominated by the statistical errors included in Eq. (9) and the uncertainty just noted for  ${}^\ell R_d^s$ . The final result for the strangeness magnetic moment of the nucleon is

$$G_M^s = -0.046 \pm 0.019 \mu_N. \quad (10)$$

The calculation of the strange quark charge radius involved the same ideas presented in Eqs. (7) and (8) but in this case the octet data are not available, so one could not use ratios of valence properties to reduce errors. Nevertheless the result,  $\langle r^2 \rangle_s^p = 0.001 \pm 0.004 \pm 0.004 \text{ fm}^2$ , was remarkably precise. Finally, we note that this technique has also been used to extract the strange magnetic form factor at finite  $Q^2$  [21].

## 2.2. Direct method

The direct calculation of the disconnected strange quark loop has proven extremely difficult in lattice QCD, which is why the indirect techniques described above were applied first. The first direct calculations [22, 23] were unable to extract robust signals for the strange form factors. However, just in the last two years, the Kentucky group has succeeded in beating down the noise to obtain a very convincing signal for the magnetic and electric strange quark form factors of the proton as a function of  $Q^2$  [24]. For the present time, the results have been reported at somewhat heavy light quark masses – corresponding to pion masses around 500 MeV. Nevertheless the strange magnetic moment found by Doi *et al.*, namely  $\mu_s = -(0.017 \pm 0.025 \pm 0.007)\mu_N$ , is in excellent agreement with the values quoted above. Indeed, a simple estimate of the effect of

moving to the physical light quark mass would make the agreement even better. The result for the strange electric charge radius was also in agreement with the value quoted above.

In conclusion, the theoretical status of the calculation of the strange electric and magnetic form factors seems to be very sound, with excellent agreement between the different techniques employed.

### 3. Experimental overview

As described above, the strange vector form factors are accessible through the precision measurement of the helicity-correlated cross section asymmetry in the elastic scattering of polarized electrons from an unpolarized target,  $A_{LR}$ . This asymmetry is small, on the order of 1-100 parts per million (ppm) for the kinematics which are typically of interest,  $Q^2 < 1 \text{ GeV}^2$ , and must be measured with a precision in the range of 10% or better. Experiments of this nature are optimized to the challenges of precision measurement of very small asymmetries, which require large high count rates and low noise to achieve statistical precision as well as a careful regard for potential systematic errors.

One common feature of all measurements of parity-violation in electron scattering is a rapid flipping of the electron beam helicity, allowing a differential measurement between opposing polarization states on a short timescale. The enabling technology for these measurements lies in the semiconductor photo-emission polarized electron source, which allows rapid reversal of the electron polarization while providing high luminosity, high polarization, and a high degree of uniformity between the two beam helicity states. Developments with the polarized source at Jefferson Lab critical to the success of this program are described elsewhere in this volume [25].

The following sections will describe a series of measurements in parity-violating in electron-nucleus scattering which took place over the first decade of the operation of Jefferson Lab: the HAPPEX measurements in Hall A and the G0 measurements in Hall C.

### 4. HAPPEX-I

The Hall A Proton Parity Experiment (HAPPEX) ran in 1998 and 1999 and pioneered parity-violation study at Jefferson Lab [26, 27, 28]. HAPPEX measured  $A_{LR}$  in elastic electron-proton scattering at the kinematics  $\langle \theta_{\text{lab}} \rangle = 12.3^\circ$  and  $\langle Q^2 \rangle = 0.477 \text{ (GeV/c)}^2$ . The Hall A High resolution spectrometers (HRS) [29] were used to focus the scattered electrons onto a total absorption shower counter in the spectrometer focal plane (Fig. 3). The HRS cleanly isolated the elastic scattered electrons, suppressing background from inelastics or low-energy secondaries. The detector in each spectrometer was instrumented with a single photomultiplier (PMT) tube. Rather than counting individual pulses, the anode current from this PMT was simply integrated over the 33 millisecond helicity periods, and the result combined with that from a consecutive window of opposite electron-beam helicity, to form the asymmetry measurement “pair”. With a detected rate of 2 MHz, the scattering rate asymmetry was measured at 15 Hz with a precision of 0.38%. The selected kinematics corresponded to the smallest angle and largest energy possible with the Hall A HRS spectrometers, which maximized the figure of merit for a first measurement.

HAPPEX-I stimulated improvements in both polarized source technology and polarimetry at Jefferson Lab. In the 1998 run the experiment used a  $I = 100 \text{ } \mu\text{A}$  beam with  $P = 38\%$  polarization produced from a bulk GaAs crystal, while in the 1999 run HAPPEX-I became the first experiment to use a strained GaAs photocathode to measure a parity-violating asymmetry in fixed-target electron scattering. This improved the figure-of-merit  $P^2I$  with  $P=70\%$  and  $I=35 \text{ } \mu\text{A}$  but also required several refinements of the techniques used to control systematic errors associated with the laser at the polarized source, in addition to the usual feedback control of the helicity-correlated charge asymmetry. The active layer of the strained photocathode was a thin ( $\sim 100 \text{ nm}$ ) layer of GaAs grown on GaAsP. The mismatch between the two lattices produced a strain in the GaS that breaks an energy-level degeneracy, allowing selective photoexcitation

of a specific polarization state and a theoretical maximum 100% electron polarization [30, 31]. During HAPPEX-I, a 70% polarization was achieved, and at the present time 85% is available due to further refinements in the technology. The strain, however, introduced an anisotropy in the quantum efficiency of the cathode, making it the dominant source of analyzing power in the system. A rotatable half-wave plate inserted downstream of the Pockels cell provided the ability to rotate the laser beam’s polarization ellipse, which reduced the sensitivity to the analyzing power, as determined by scans of the helicity-correlated position differences and charge asymmetries versus the angle of this half-wave plate [28]. A half-wave plate upstream of the Pockels cell was aligned to invert the sign of incident linear polarization, which toggled the sign of the laser circular polarization, and therefore the electron beam helicity, relative to the Pockels cell voltage settings. The state of this waveplate was toggled every 24–48 hours. This method of slow helicity reversal provided a way to cancel out some sources of possible systematic errors, including false asymmetries from electronics pickup and certain helicity-correlated beam asymmetries.

During HAPPEX-I the Hall A Compton polarimeter [32] was commissioned and provided, for the first time, a continuous monitoring of the electron beam polarization with a run-to-run relative error of less than 2%, and a total error on absolute polarization averaged over the run of 3.3%. The dominant systematic uncertainty for this polarimeter lay in the corrections of the theoretical analyzing power for realistic detector performance. A second polarimeter was also used in Hall A, based on Møller scattering from a polarized ferromagnetic foil [29]. The Møller polarimetry results carried a total uncertainty of 3.2%, primarily due to uncertainty in the polarization of the electrons in the target foil. This polarimeter was invasive and could not be used as a continuous monitor, but results from measurements interspersed with data-taking were in good agreement with the results from the Compton polarimeter. These results agree also with measurements by a third polarimeter, based on Mott scattering in the 5 MeV region of the injector, which was quoted with a total error of about 7%.

HAPPEX-I yielded a very clean physics result and was published within a year after the experiment was completed. Due to the high-quality of the Jefferson Lab polarized source and superconducting accelerator, the systematic errors associated with the beam were found to be negligible compared to the statistical error. The accuracy of the result was sufficient to rule out several theoretical estimates of strangeness effects at moderately high  $Q^2$  where it was thought the effects might have been large. The distribution of window-pair asymmetries are shown in Fig. 4; the distribution is Gaussian over 6 orders of magnitude, with a width consistent with counting statistics. Uncorrected asymmetries from the 1999 running period are shown in Fig. 5, averaged over the 24-48 hour periods between half-wave plate insertions. The measured asymmetry flips sign cleanly with the insertable half-wave plate. After all corrections, the HAPPEX-I physics asymmetry was found to be

$$A = -15.05 \pm 0.98 \pm 0.56 \text{ ppm}, \quad (11)$$

where the first error is statistical and the second error is systematic. This latter includes the errors in the beam polarization, background subtraction, helicity-correlated beam properties, and  $Q^2$ . Using this result, along with the calculated  $G_A^p$  [10] and the known values of the proton and neutron form factors, the experiment determined the linear combination of strange form factors  $G_E^s + \eta G_M^s$  where  $\eta = \tau G_M^{\gamma p} / \epsilon G_E^{\gamma p} = 0.392$  at the given kinematics. Thus,

$$G_E^s + \eta G_M^s = 0.014 \pm 0.020 \pm 0.010, \quad (12)$$

where the first error is the total experimental error (statistical and systematic errors added in quadrature) and the second error is the error due to the “ordinary” electromagnetic form factors, which was dominated by the uncertainty in  $G_M^n$ .

The clean and rapidly published result of HAPPEX-I, encouraged the development of further, more accurate and ambitious parity-violation measurements at Jefferson Lab.

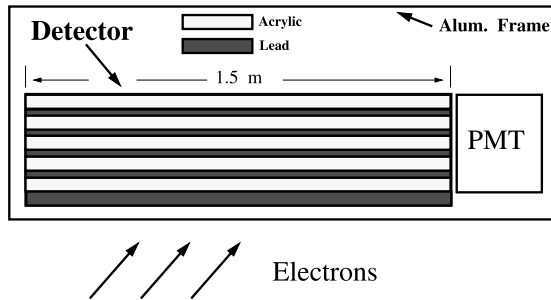


**Figure 3.** Schematic of the focal plane detector used by HAPPEX-I. The scattered electrons strike a lead-acrylic shower counter whose light is collected by a PMT and integrated over a helicity period.

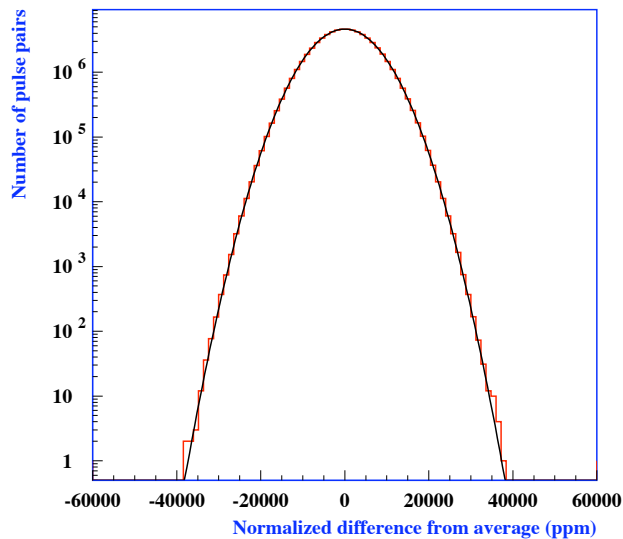


**Figure 4.** The window pair asymmetries in ppm for HAPPEX-I, normalized by the square root of beam intensity, with the mean value subtracted off. The curve is a Gaussian fit.

### 5. The second generation HAPPEX experiments

The second generation HAPPEX experiments ran in 2004 [33, 34] and 2005 [35]. Similar to the original HAPPEX experiment in technique, they measured forward-angle elastic scattering from the proton and from the  ${}^4\text{He}$  nucleus using the HRS to cleanly separate the elastic events. A smaller scattering angle was achieved, about  $6^\circ$ , by using a superconducting septum dipole magnet to bend the small scattering angles into the  $12.5^\circ$  minimum acceptance for the HRS. The figure of merit was again optimized at the maximum momentum accepted by the HRS, with a  $Q^2 \sim 0.1 \text{ GeV}^2$ .

Elastic scattering from an isoscalar  $0^+$  nucleus does not allow contributions from magnetic or axial-vector currents. At tree level, the parity-violating asymmetry for scattering from  ${}^4\text{He}$



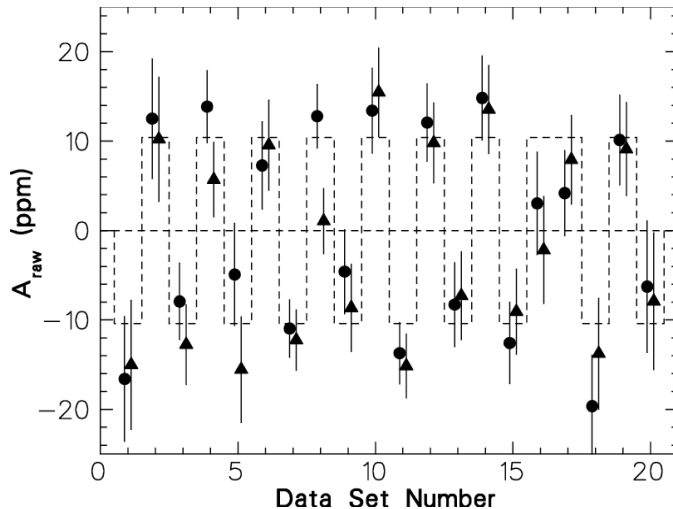


**Figure 5.** Raw asymmetries (ppm) for HAPPEX-I in the 1999 run. Each data set is  $\sim 1$  day of running. The circles are for the left spectrometer, triangles for the right spectrometer. The step pattern represents the insertion and removal of the half-wave plate which reverses the sign.

can be written as

$$A_{PV}^{\text{He}} = \frac{G_F Q^2}{4\pi\alpha\sqrt{2}} \left( 4\sin^2\theta_W + \frac{2G_E^s}{G_E^p + G_E^n} \right). \quad (13)$$

With sufficient precision, measurement of this asymmetry isolates the strange electric form factor  $G_E^s$  alone. For  ${}^4\text{He}$ , nuclear model corrections to the asymmetry due to isospin mixing [36, 37],  $D$ -state admixtures [38], and meson-exchange contributions [39] are all negligible at low  $Q^2$ . In addition to the independence from nuclear models,  ${}^4\text{He}$  provided a particular advantage of a deeply-bound ground state, which separated the nearest inelastic level by about 20 MeV and allowed the HRS to easily isolate elastic scattering. The strong  $Q^2$  dependence of the Mott cross section supports the figure-of-merit in the region  $Q^2 \sim 0.1 \text{ GeV}^2$ . Measurements at significantly higher  $Q^2$  would be problematic, both due to figure-of-merit and control of the nuclear corrections.

The measurements used 20 cm long cryogenic targets, with  $\sim 3 \text{ GeV}$  electron beam at currents from 35 to 55  $\mu\text{A}$ . The targets were a novel design, using a transverse flow of cryogen across the beam axis to avoid localized heating in regions of low fluid flow velocity. A superconducting septum magnet captured scattered flux from around  $6^\circ$  into the HRS acceptance, where the elastically scattered electrons in each spectrometer were focused onto a brass/quartz Cerenkov counter. The signal from each counter was integrated over periods of about 33 milliseconds, resulting in an asymmetry measurements made at a rate 15 Hz with a precision of 540 ppm for the  ${}^1\text{H}$  target and 1130 ppm for the  ${}^4\text{He}$  target.

The high precision of these measurements required careful control of helicity-correlated beam asymmetries. Detailed studies of the laser optics of the polarized source led to improved characterization of the optical elements, as well as an improved algorithm for aligning the electro-optic Pockels cell which is used to create the fast helicity flip. Care was also taken to avoid magnifying any helicity-correlated orbit changes during beam acceleration and transport. As a result, the helicity-correlated position differences, averaged over the course of the run, was held to less than 2 nm for the Hydrogen measurement.

For the Helium measurement, electronics meant to drive additional helicity-correlated feedback systems created an unanticipated problem. An electrical control signal, indicating the

beam polarization state to a hardware driver on the source laser table, interacted with devices on the electron beam line to steer the electron beam. This led to large position differences, as large as 600 nm at the target, which were in fact related only to the electrical signal which indicated helicity, and not to the actual helicity of the electron beam. This was proven by the observation that the differences existed even when the electron beam was left unpolarized by switching off high-voltage to the Pockels cell used to create the laser polarization state. Changing the polarity of this control signal input to the suspect system was also seen to toggle the sign of the steering effect. Careful checks revealed no electrical contamination of the data acquisition in the experimental hall; this effect was confined to the observed steering in the injector. Before the hardware driver was switched off to remove this effect, additional production data was first collected with the control signal flipped to provide a degree of cancellation for effects of this electrical leakage. Because this effect related to the control signal and not to laser or electron beam polarization, it was also seen to cancel well when averaged over the half-wave plate helicity reversal.

In addition to controlling the beam asymmetries, a correction for measured helicity-correlated beam asymmetries was applied. The sensitivities, that is, the changes in detected rate with changing beam parameters, were calibrated using periodic, deliberate beam modulation. Air core magnets in the arc leading to the hall moved the beam in a step-wise, sawtooth pattern, spanning the space of both position and angle at the target. An energy vernier was used to modulate the energy as well. Measuring the response of beam monitors and the detector to these individual modulations allowed for a measurement of the slopes which enforced the orthogonality of the motions, and avoided systematic misinterpretations of the sensitivities due to correlations in the beam motion or electronics noise. The results were consistent with expectations from simulation. The small corrections for helicity-correlated beam asymmetries, and the estimated systematic uncertainty in those corrections, were based on the sensitivities measured using this beam modulation.

The detector, which relied on Cerenkov light generated by high-energy leptons in an electromagnetic shower, preferentially collected light from the direction of primary tracks in the spectrometer. This directional sensitivity and low sensitivity to soft backgrounds, along with the detector location in the heavily shielded detector hut of the HRS, provided a very low background measurement. The largest background in the measurement, due to quasi-elastic scattering from the aluminum windows of the target, was measured to be  $0.8 \pm 0.25\%$  of the signal from  $^1\text{H}$  and  $1.8 \pm 0.2\%$  for  $^4\text{He}$ . This fraction was directly bounded by measurements of the production target with varying cryogenic gas densities. The uncertainty in the background rate and in the asymmetry of the background (due to possible inelastic contributions which would not be detectable at very low fractional rate) combined for a total uncertainty of 1.3% for  $^1\text{H}$  and 0.6% for  $^4\text{He}$ . Spectra of the high-resolution kinematic reconstruction in the HRS gave a range of  $0.15 \pm 0.15\%$  for the quasielastic and inelastic fractional contributions to the  $^4\text{He}$  signal. Additional backgrounds due to rescattering of inelastics in the spectrometer were estimated using dedicated calibration runs to measure rescattering probabilities. Rescattering from exposed polarized iron in the spectrometer was estimated to be negligible. The net correction for all backgrounds was  $0.6 \pm 1.4\%$  for  $^1\text{H}$  and  $2.8 \pm 0.8\%$  for  $^4\text{He}$ .

The measured asymmetry was corrected for the electron beam polarization using a Compton polarimeter with a precision of 1%. The dominant systematic uncertainty in the Compton polarimetry arises from the determination of the analyzing power with realistic effects from detector resolution and energy calibration. The key to high precision was the extremely precise beam tune, where the beam halo was so well contained at the Compton electron detector that the silicon strip detector could frequently make measurements with active strips only 5 mm from the primary electron beam. This allowed a precision energy calibration of the electron detector, through measurement of the location of the cross section kinematic limit (the ‘‘Compton edge’’)

and the zero-crossing of the asymmetry. The energy calibration of the electron detector could then be transferred to the photon detector through spectra measured with an electron-photon coincidence trigger. This technique reduced the calibration errors relative to previous analyses using the Compton polarimeter [32], with the final uncertainty estimated at the level of 1%. Within the quoted uncertainties, the results were consistent (though somewhat more precise) with the measurements from the Møllerpolarimeter in the hall and the Mott polarimeter in the injector.

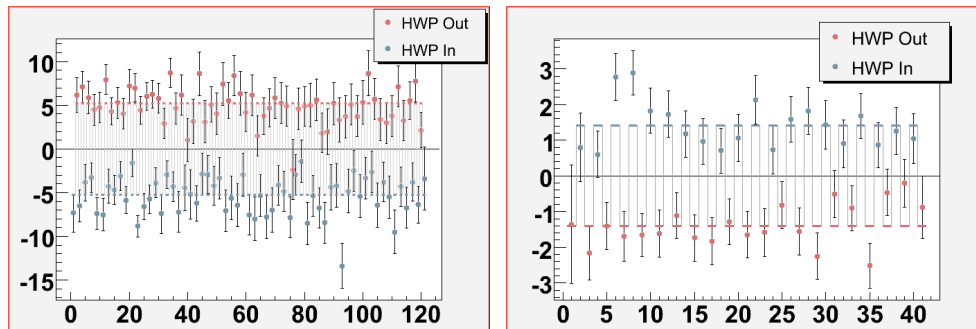


**Figure 6.** Corrected asymmetries (ppm) for HAPPEX-II in the 2005 run [35]. Each data point represents the measured asymmetry, averaged over the two spectrometers, for a period between half-wave plate reversals, for the  $^4\text{He}$  (left) and  $^1\text{H}$  (right) measurements. The step pattern represents the insertion and removal of the half-wave plate which reverses the sign of the asymmetry. Vertical axis labels are in units of parts per million, horizontal axis is the index for periods between half-wave plate changes.

In order to interpret the measured asymmetry, an accurate determination of the accepted kinematics is required. A thin water target with steel beam window foil was used to determine the angular alignment of the spectrometer by observing the momentum difference between hydrogen elastic scattering and elastic or inelastic scattering from heavier nuclei, as shown in Fig. 7. Results from this calibration method agreed well with an independent determination based on survey of a pinhole collimator, which could be inserted between the target and any magnetic elements of the spectrometer. As a result, uncertainties in the kinematics calibration were bounded to less than 1%, leading to a 1.7% systematic error of  $^1\text{H}$  and 0.9% for  $^4\text{He}$ . An additional correction of  $2.1\% \pm 0.2\%$  for the hydrogen measurement, accounting for the finite range of  $Q^2$  accepted, was determined using Monte Carlo simulation. The  $^4\text{He}$  measurement is exactly proportional to  $Q^2$  at tree level and required no such correction.

The published results for the HAPPEX-II  $^1\text{H}$  and  $^4\text{He}$  measurements are given in Table 2. The extracted results for the strange form factors from the hydrogen measurements are necessarily dependent on the values of the electromagnetic form factors, which introduces an uncertainty into the theoretical expectation for the asymmetry in the absence of the strangeness contribution. This extraction is also very weakly dependent on the poorly known “anapole moment” radiative correction, which influences the axial term. The extraction shown here uses the Zhu *et al.* [10] estimate for this correction and corresponding uncertainty. Under the simple assumption that  $G_E^s$  is proportional to  $Q^2$  and  $G_M^s$  is varying slowly enough in this region to be considered constant, the electric and magnetic strange vector form factors can be extracted from these results to be:  $G_E^s = -0.005 \pm 0.019$  and  $G_M^s = 0.18 \pm 0.27$ , with a correlation coefficient of -0.87.

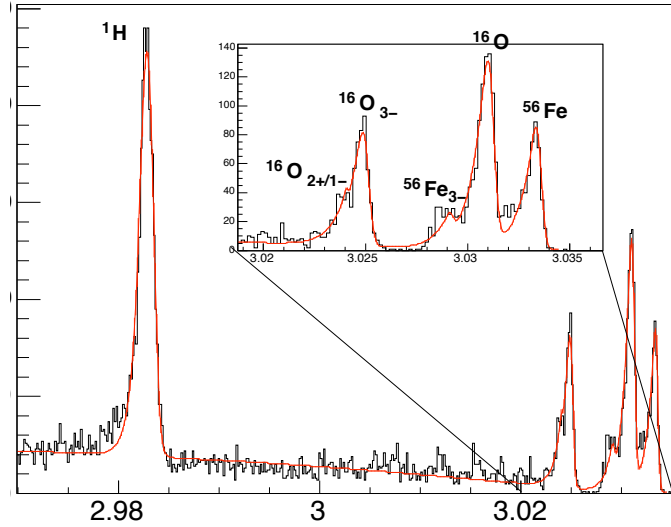


**Figure 7.** Reconstructed momentum spectrum for the HAPPEX-II watercell target (horizontal axis in units of GeV). Iron and oxygen states can be precisely resolved; measuring the momentum difference between these states and elastic proton scattering provides an accurate measurement of the scattering angle, with greatly reduced sensitivity to uncertainty in the primary beam momentum and spectrometer momentum calibration. The availability of each state from a single target reduces the uncertainties in target energy loss corrections. Using this technique, scattering angles were calibrated with an accuracy of 0.2 mrad in an entirely beam based measurement. Results agreed with survey reports on the experimental apparatus.

Correction (ppb)	Helium	Hydrogen
Beam Asymmetry	$183 \pm 50$	$10 \pm 17$
Target window bkg.	$113 \pm 32$	$7 \pm 19$
Helium QE bkg.	$12 \pm 20$	–
Rescattering bkg.	$20 \pm 15$	$2 \pm 4$
Nonlinearity	$0 \pm 58$	$0 \pm 15$
Scale Factor	Helium	Hydrogen
Acceptance Scale Factor $K$	$1.000 \pm 0.001$	$0.979 \pm 0.002$
$Q^2$ Scale	$1.000 \pm 0.009$	$1.000 \pm 0.017$
Polarization $P_b$	$0.844 \pm 0.008$	$0.871 \pm 0.009$

**Table 1.** Corrections and systematic error summary for HAPPEX-II and HAPPEX-Helium [35].

## 6. The G0 experiment

The G0 experiment [40, 41] measured the forward proton asymmetries and backward asymmetries for both the proton and deuteron to provide, within a single apparatus, a complete set of measurements over a broad range of kinematics from which the electric and magnetic strangeness form factors, as well as the axial neutral weak current of the nucleon, could be extracted.

### 6.1. G0 forward

The forward-angle G0 experiment [40] ran in Hall C in 2003 and 2004, using a novel 8-coil, superconducting toroidal magnet to focus recoil protons from the elastic electron-proton

dataset	$Q^2$ [GeV <sup>2</sup> ]	Result	
2004 <sup>4</sup> He	0.077	$A_{NVS}^{\text{He}} = +7.48$ ppm	$A_{PV}^{\text{He}} = +6.72 \pm 0.84 \pm 0.21$ ppm
		$G_E^s = -0.038 \pm 0.042 \pm 0.010$	
2005 <sup>4</sup> He	0.091	$A_{NVS}^{\text{He}} = +6.37$ ppm	$A_{PV}^{\text{He}} = +6.40 \pm 0.23 \pm 0.12$ ppm
		$G_E^s = 0.002 \pm 0.014 \pm 0.007$	
2004 <sup>1</sup> H	0.099	$A_{NVS}^{\text{H}} = -1.43 \pm 0.11$ ppm	$A_{PV}^{\text{H}} = -1.14 \pm 0.24 \pm 0.06$ ppm
		$G_E^s + 0.08G_M^s = 0.030 \pm 0.025 \pm 0.006 \pm 0.012$	
2005 <sup>1</sup> H	0.109	$A_{NVS}^{\text{H}} = -1.66 \pm 0.05$ ppm	$A_{PV}^{\text{H}} = -1.58 \pm 0.12 \pm 0.04$ ppm
		$G_E^s + 0.09G_M^s = 0.007 \pm 0.011 \pm 0.004 \pm 0.005$	

**Table 2.** Published results from the HAPPEX-II measurements on hydrogen and helium [35]. Error bars are listed in order for statistical and systematic uncertainties, and for form factor uncertainties where appropriate.

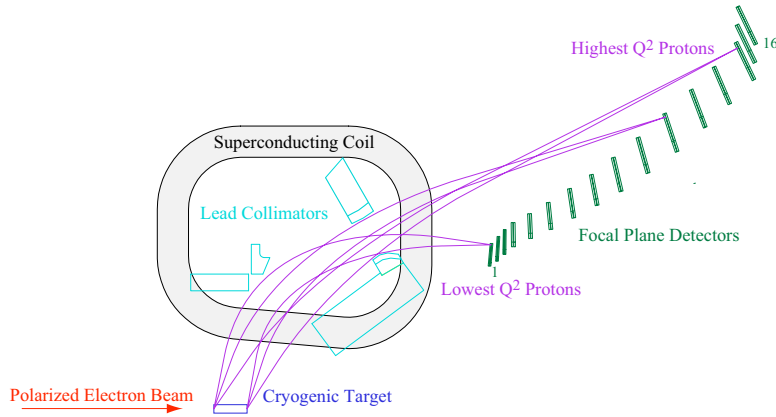


**Figure 8.** Schematic of the G0 spectrometer as used in the forward angle experiment.

scattering onto one of eight arrays of plastic scintillator detectors located outside the magnet. A  $40 \mu\text{A}$ , 74% polarized beam from a strained GaAs polarized source was used, with 32 ns pulse timing, rather than the standard 2 ns, to allow for precise time-of-flight measurements which discriminated against various backgrounds. The delivery of high average beam current with this pulse timing required very high peak currents, and therefore provided significant challenges in accelerator physics due to the large space-charge effects in each bunch. The acceptance was about 0.9 steradians at recoil angles centered around  $70^\circ$ . With a beam energy of 3 GeV the acceptance corresponded to a  $Q^2$  range  $0.12 \leq Q^2 \leq 1.0 \text{ GeV}^2$ . Each of the eight detector arrays consisted of 16 different detectors, the Focal Plane Detectors (FPD<sub>*i*</sub>). The detectors were each a two-layer sandwich of scintillators, and each layer was read out by two phototubes. Each detector in the range distinguished a unique bin in  $Q^2$ , with the exceptions of the range  $0.44 \leq Q^2 \leq 0.88 \text{ GeV}^2$ , which all lay in FPD 15 and was segmented using time-of-flight, and FPD 16, which was located beyond the kinematic limit for elastic scattering, and was used for monitoring backgrounds. The  $Q^2$  acceptance for each detector was calibrated to 1% precision using time-of-flight measurements between  $\pi^+$  and elastic protons.

Rather than an integrating method, as adopted by the HAPPEX experiments, the G0

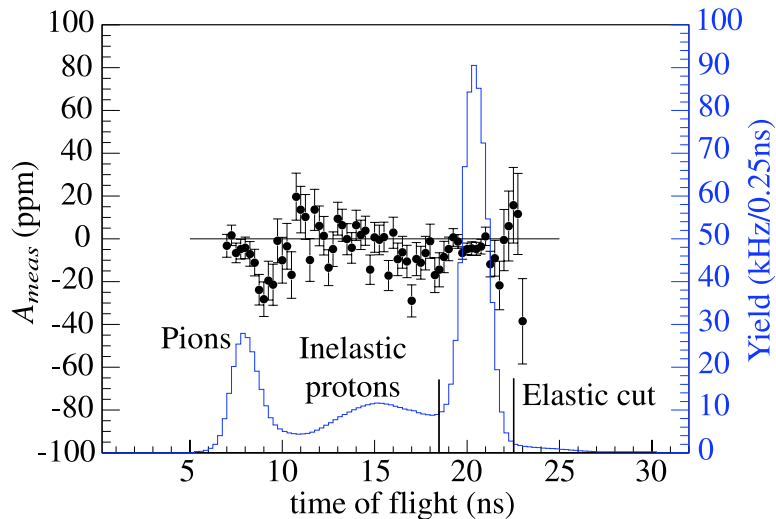


**Figure 9.** The time-of-flight distribution (histogram) for a typical detector (FPD 8) in the forward angle G0 experiment, along with the raw measured asymmetries (points with statistical errors).

experiment used a counting method to form the experimental asymmetries. Custom electronics allowed time-of-flight spectra to be accumulated for each helicity state. An asymmetry was then formed bin-by-bin in the spectra for each FPD. The pattern of fast helicity reversal was, unlike the HAPPEX experiments, formed not in pairs, but in quartets, where each quartet was either the sequence of helicity states LRRL or RLLR (L and R referring to left and right handed helicity, respectively). The quartet structure was chosen to exactly cancel the effect of any linear drifts in, for example, detector threshold or gain. The measured asymmetry was formed for each helicity quartet, *e.g.*  $A_{\text{meas}} = \frac{Y_L - Y_R - Y_R + Y_L}{Y_L + Y_R + Y_R + Y_L}$  for LRRL, where  $Y_L$  and  $Y_R$  are the measured yield in each helicity window. This measured asymmetry can be expressed as  $A_{\text{meas}} = (1-f)A_{\text{el}} + fA_{\text{b}}$  where  $A_{\text{el}}$  is the raw elastic asymmetry,  $A_{\text{b}}$  the background asymmetry and  $f$  the background fraction.

The elastic protons were identified by time-of-flight relative to the electron beam bunch; this allowed the rejection of protons from inelastic scattering, and faster particles such as the  $\pi^+$ , as shown in Fig. 9. Background yields and asymmetries were measured concurrently and used to correct the elastic asymmetries. In the region of the elastic peak, the background is essentially composed only of inelastic protons. Background was subtracted in each detector using a simultaneous fit of the time-of-flight yield and asymmetry spectra near the elastic cut. For this fit, the yield is modeled with a Gaussian elastic peak on a polynomial background, while the elastic asymmetry is fit to a constant and the background to a quadratic function. For higher number detectors the background asymmetry becomes positive, due to a small number of protons from the weak decays of hyperons, that scatter in the magnet, leading to corrections which were 20-110% of the final result. The uncertainties in these corrections were estimated from the variation in results using a variety of different models for the background asymmetries and yields. These corrections lead to a significant correlation between the estimated systematic uncertainties for data points in the range  $Q^2 > 0.3 \text{ GeV}^2$ .

The beam polarization was measured using a Møller polarimeter [42] to a precision of 1%. Radiative corrections of 1–3% were performed using simulation. Small corrections for electronics deadtime were made on the basis of the observed dependence of the yield on the beam current.

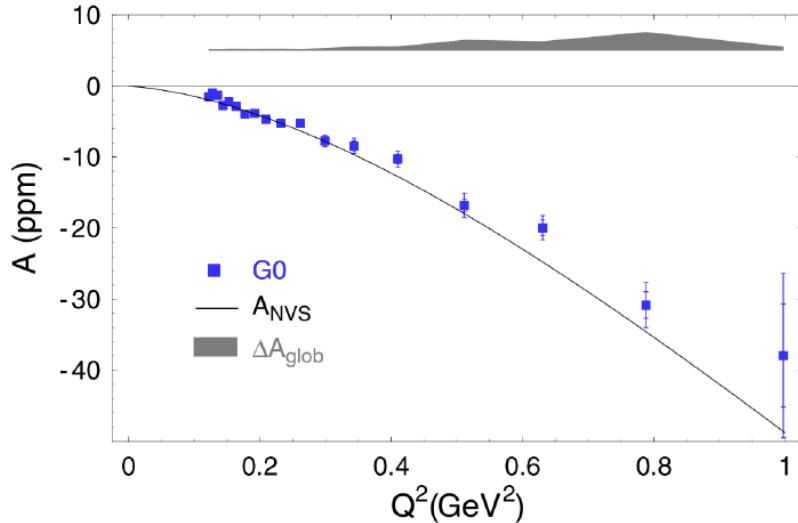


**Figure 10.** Results from the G0 forward angle measurements of  $A_{LR}$  in elastic electron-proton scattering [40]. Data points are shown with statistical and point-to-point systematic error bars combined, while the shaded band represents the magnitude of systematic errors which are highly correlated between the data points. The curve  $A_{NVS}$  represents the expected value of  $A_{LR}$  in the absence of strange contributions to the vector form factors.

An additional correction was required for an asymmetric “leakage” beam. This was a problem unique to the non-standard time structure: some fraction of the total beam to Hall C was leakage beam, primarily tails of the beam intended for the other two halls, which arrived with the standard 499 MHz time structure and was recorded by the 1497 MHz beam current monitors along with the expected G0 beam. Being off-time, elastic scattered protons from this leakage beam did not contribute to the signal in the elastic cut, leading to a mis-match between the measured beam current asymmetry and the beam current which contributed to the accepted signal. Although a small fraction of the total beam, there was a strong helicity dependence for this leakage beam. The correction for this leakage beam asymmetry was  $0.7 \pm 0.1$  ppm, and nearly uniform over all detectors.

Results for the final measured asymmetries after all corrections are shown as a function of  $Q^2$  in Fig. 10. For each  $Q^2$  point, the combination of strangeness form factors  $G_E^s + \eta G_M^s$  as a function of momentum transfer was obtained, as discussed in Section 7 and shown in Fig. 12, where  $\eta(Q^2) = \tau G_M^p / \epsilon G_E^p$ . The results were in excellent agreement with the earlier HAPPEX-I measurement [28], and displayed a noticeable bias toward a positive strangeness contribution at higher  $Q^2$ , which prompted the next round of high-precision experiments at Jefferson Lab and at Mainz.

### 6.2. G0 backward

The G0 backward-angle phase experiment was conducted in Hall C at Jefferson Lab in 2006 and 2007. The G0 superconducting toroidal spectrometer was turned  $180^\circ$  around with respect to the beam direction compared to the forward-angle configuration, in order to detect the electrons scattered at an angle of about  $110^\circ$  from 20 cm liquid hydrogen and deuterium targets. Polarized electron beams with currents up to  $60 \mu\text{A}$  and energies of 359 and 684 MeV were generated with a strained GaAs polarized source. In this phase, the standard Jefferson Lab time structure was used for the beam, as time-of-flight was not useful for separating the scattered electrons

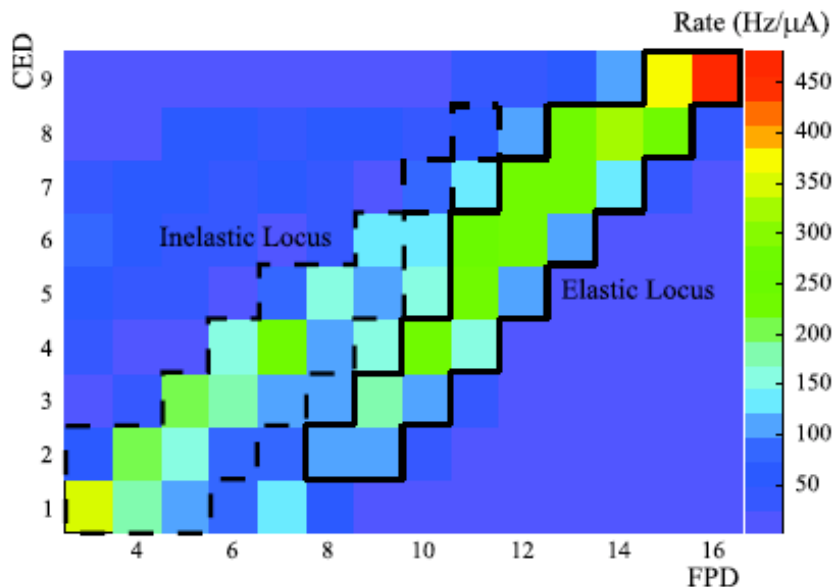


**Figure 11.** The distribution of measured yields from the backward-angle phase of G0, as a function of FPD and CED, for hydrogen data taken at a beam energy of 687 MeV. (Note: FPDs 1 and 2 are not used,) Electrons from elastic (inelastic) scattering are in the upper right (lower left).

from backgrounds. The quartet helicity reversal pattern was adopted as for the forward-angle experiment. The average beam polarization was  $85.8 \pm 2.1(1.4)\%$  at the lower (higher) incident energy. In this phase, the focal-plane detector array (FPD<sub>i</sub>) that was used in the forward angle measurement was augmented with a second array of scintillators, near the exit of the magnet (CED<sub>i</sub>). Coincidences between these two scintillator arrays allowed electrons from elastic and inelastic scattering to be distinguished, as shown in Figure 11.

Additionally, in each octant an aerogel Cerenkov detector was added in order to separate the electrons from the copious background from pions. The Cerenkov detectors had a pion rejection factor  $\geq 85\%$  and an electron efficiency of about 85%. The backgrounds in the region of the elastic locus (see Fig. 11) amounted to 10–15% of the signal. In the elastic locus, the aluminum target windows was the dominant background with misidentified  $\pi^-$  and electrons from  $\pi^0$  conversion also contributing. The aluminum fraction was measured using runs with cold gaseous hydrogen in the target and the pion contamination was determined from dedicated time-of-flight runs and pulse-shape analysis. Additionally, an acceptance study was performed by sweeping the field of the toroid  $\pm 40\%$  of the nominal setting and comparing the measured yield in each coincidence cell with Monte Carlo simulation using GEANT. The aluminum asymmetry was taken to be the same as that of the deuteron (both effectively quasi-elastic scattering only) with an additional uncertainty of 5% for nuclear effects. The asymmetry for the pion production background was small ( $< 1$  ppm) and was measured concurrently with that for the electrons. The background corrections are small because the background asymmetries generally have values close to those of the elastic asymmetry, or, otherwise, the fraction is small.

All asymmetries were corrected for measured rate-dependent effects. For elastic scattering, dead-time corrections generally dominated those from accidentals and amounted to  $\sim 15\%$  of the yield based on the measured beam current dependence, and led to an uncertainty of about



**Table 3.** G0 backward-angle: corrections to the measured asymmetry and the final physics asymmetries. Rate and “Other” corrections are additive; electromagnetic radiative corrections are multiplicative. “Other” corrections include those for helicity-correlated beam parameters, the transverse component of beam polarization, and two-boson exchange. Not listed is the common multiplicative correction for the beam polarization,  $1.16 \pm 0.02$ . The uncertainties for the asymmetries are statistical, point-to-point systematic and global systematic, respectively.

Target	$Q^2$ (GeV <sup>2</sup> )	Rate (ppm)	Other (ppm)	EM Radiative	$A_{\text{phys}}$ (ppm)
H	0.221	$-0.31 \pm 0.08$	$0.22 \pm 0.08$	$1.037 \pm 0.002$	$-11.25 \pm 0.86 \pm 0.27 \pm 0.43$
D	0.221	$-0.58 \pm 0.21$	$0.06 \pm 0.10$	$1.032 \pm 0.004$	$-16.93 \pm 0.81 \pm 0.41 \pm 0.21$
H	0.628	$-1.28 \pm 0.18$	$0.29 \pm 0.11$	$1.037 \pm 0.002$	$-45.9 \pm 2.4 \pm 0.8 \pm 1.0$
D	0.628	$-7.0 \pm 1.8$	$0.34 \pm 0.21$	$1.034 \pm 0.004$	$-55.5 \pm 3.3 \pm 2.0 \pm 0.7$

0.5 ppm in the asymmetries. In the high-energy deuteron measurement, accidentals from pion signals in the scintillators in coincidence with random signals from the Cerenkov dominated the correction. In this case, the correction to the asymmetry was  $7.0 \pm 1.8$  ppm. Helicity-correlated intensity changes were corrected with active feedback to about 0.3 ppm. Corrections to the measured asymmetry for residual helicity-correlated beam current, position, angle and energy variations of at most  $0.2 \pm 0.07$  ppm were applied *via* linear regression. Electromagnetic radiative corrections of  $(3 - -3.5) \pm 0.3\%$  and small two boson exchange effects (1%) were also applied to the asymmetries. Table 3 shows the corrections to the raw elastic asymmetry,  $A_{\text{el}}$ , as well as the final asymmetries  $A_{\text{phys}}$  and their statistical and systematic uncertainties. The extraction of strange form factors from these data is discussed in the next section.

## 7. Summary and outlook

The HAPPEX and G0 experiments at Jefferson Lab have provided precision measurements of the weak form factors of the nucleon over a range of  $Q^2 < 1$  GeV<sup>2</sup>. The global data set on forward-angle scattering from the proton, which is shown in Fig. 12, also includes measurements from the PVA4 collaboration at the Mainz Microtron [43, 44]. For each data point, the combination of strangeness form factors  $G_E^s + \eta G_M^s$  as a function of momentum transfer was obtained, where  $\eta(Q^2) = \tau G_M^p / \epsilon G_E^p$ . This combination represents the net contribution of the strange form factors to  $A_{\text{LR}}$  in each measurement. Taken as a whole, this data set systematically appears to suggest a small but positive strange form factor combination, however, it does not establish a clear, statistically significant signal. At low  $Q^2$ , the highest precision measurements constrain contributions to be very near zero. At higher  $Q^2 > 0.5$  GeV<sup>2</sup>, there remains a suggestion of a possibly measurable contribution.

Figure 13 shows published data obtained at  $Q^2 \sim 0.1$  GeV<sup>2</sup>. In addition to forward-angle data from Jefferson Lab and PVA4 [43, 44] collaborations, this figure displays results from the HAPPEX <sup>4</sup>He measurement and backward-angle measurements from SAMPLE at MIT-Bates [45]. Each measurement appears as a band, representing the central value and  $1\sigma$  error bar for the specific combination of  $G_E^s$  and  $G_M^s$ . The G0 result plotted here is an average of 3 published data points from the forward-angle data set, covering  $Q^2 = 0.12 - 0.14$  GeV<sup>2</sup>. For each of these measurements the anapole radiative correction to the axial form factor is included with the uncertainty as prescribed by theoretical expectation [10]. These data can be fit to extract  $G_E^s = -0.006 \pm 0.016$  and  $G_M^s = 0.33 \pm 0.21$ , with a correlation coefficient of  $-0.83$  [46]. Also displayed, as the small, filled ellipse, is the result of the Adelaide indirect lattice calculation described in Section 2.1.

In the absence of reliable theoretical guidance on the  $Q^2$  variation of the strange form factors,

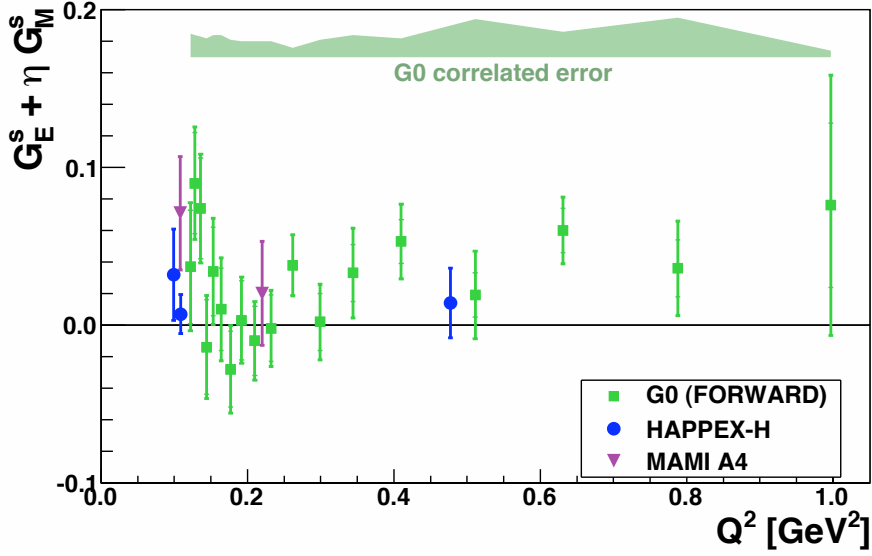


**Figure 12.** Results from world data measuring  $A_{PV}$  from forward-angle scattering from the proton, plotted as the net strange quark contribution  $G_E^s + \eta G_M^s$ . Here  $\eta = \tau G_E^p / \epsilon G_M^p$ , and is approximately equal to  $Q^2$  over this plot. In addition to HAPPEX and G0, published results from the PVA4 experiment at MAMI at  $Q^2 = 0.1$  and  $0.23 \text{ GeV}^2$  are shown [43, 44].

fits to the global data set have used a first-order power-expansion in  $Q^2$  to fit all data up to about  $Q^2 < 0.3 \text{ GeV}^2$ . The result of such a fit [47] is shown as the solid elliptical contour (68% confidence level) in Fig. 13. This fit does not include the backward-angle results at  $Q^2 \sim 0.22 \text{ GeV}^2$  from G0 and A4, and applies no theoretical constraint on the axial form factor contribution which includes the anapole moment correction. These results are statistically consistent with fits of the data near  $Q^2 = 0.1 \text{ GeV}^2$  which incorporate theoretical limits on the anapole correction, as shown above. However, the inclusion of data at higher  $Q^2$  tends to draw the central value of the fit to zero, implying either a strong  $Q^2$  dependence to the strange form factors or that the suggested deviation at  $Q^2 \sim 0.15 \text{ GeV}^2$  is a statistical fluctuation.

Figure 14 shows the strange form factors  $G_E^s$ ,  $G_M^s$ , and the isovector axial form factor  $G_A^e(T = 1)$ , extracted from the combination of the G0 backward angle and forward-angle asymmetries at  $Q^2 = 0.221$  and  $0.628 \text{ GeV}^2$  [40, 41]. These results utilize a simple interpolation of the G0 forward angle measurements to the exact  $Q^2$  of the backward angle data. The Kelly [48] parameterization of the nucleon electromagnetic form factors,  $G_{E,M}^{p,n}$  was adopted for these determinations in order to be consistent with the deuteron model used [49]. Figure 14 also shows the extraction of  $G_E^s$ ,  $G_M^s$ ,  $Q^2 = 0.1 \text{ GeV}^2$  described above [46]. Note that the PVA4 points shown [50], in contrast to the G0 results, are not based on measurements on deuterium and therefore assume a value for  $G_A^e(T = 1)$  determined by theoretical expectation Zhu *et al.* [10] shown in Fig. 14c), and a dipole form factor with a mass parameter of  $1.032 \text{ GeV}$ .

Taken as a whole, all these data clearly suggest that the strange vector form factors are a small contribution to the charge and magnetization distributions of the proton, consistent with the recent direct and indirect lattice QCD determinations, discussed above. There remains a suggestion in the experimental data that a significant contribution may be measurable at  $Q^2 \sim 0.6 \text{ GeV}^2$ . This suggestion will be tested by the HAPPEX-3 experiment [51], which ran in 2009, measuring at a  $Q^2 \sim 0.62 \text{ GeV}^2$  and using techniques developed during the preceding HAPPEX experiments. Benefiting from the high luminosity and polarization available at

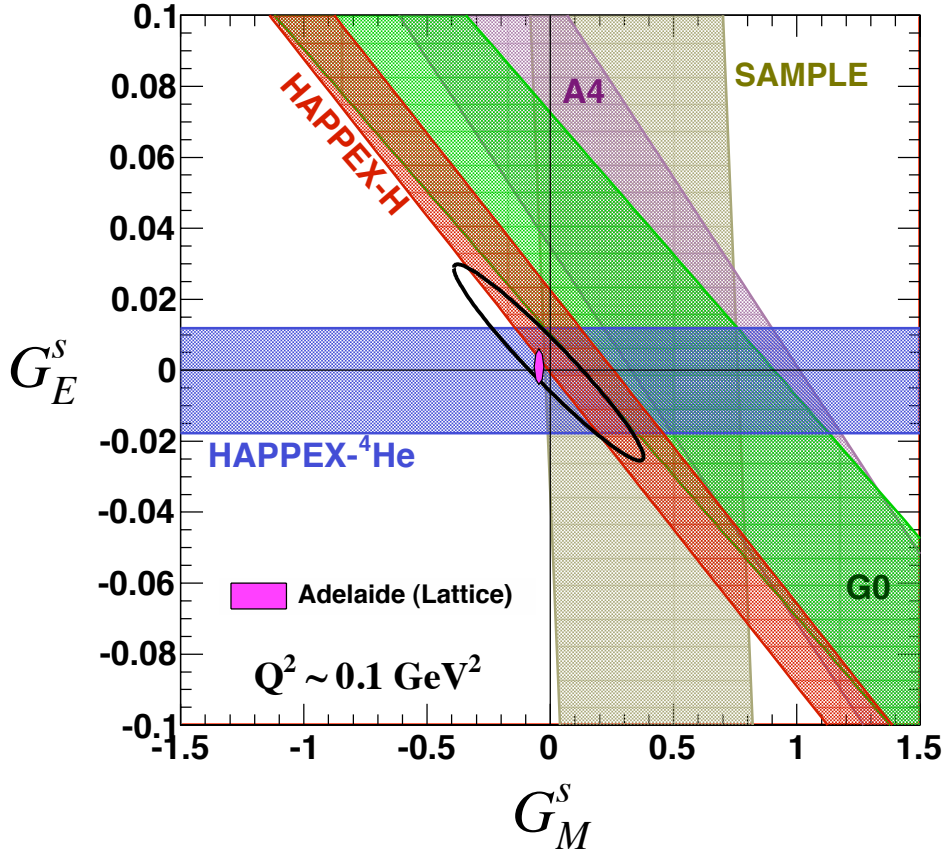


**Figure 13.** Measurements of  $G_E^s$  and  $G_M^s$  in the region of  $Q^2 = 0.1 \text{ GeV}^2$ . Each band represents the  $1\sigma$  error bar for a unique combination of the strange form factors. Results of a recent QCD calculation from the Adelaide [13, 14, 21] is shown as a filled ellipse. As described in the text, the 68% confidence level contour of a global fit [47] incorporating data beyond what is shown in this plot is shown as a solid elliptical contour.

Jefferson Lab, along with improved alignment and polarimetry techniques, HAPPEX-3 will measure  $G_E^s + 0.52G_M^s$  with an error bar  $\pm 0.010$  (stat)  $\pm 0.005$  (syst)  $\pm 0.010$  (ff), where the latter uncertainty arises from imperfect knowledge of the electromagnetic form factors. This result will greatly improve the precision of the  $G_E^s$ ,  $G_M^s$  extraction at this  $Q^2$ , providing an opportunity to establish a clear, statistically significant non-zero signal.

This program of measurement was originally motivated by theoretical suggestions of potentially large contributions of strange quarks to the nucleon vector form factors. Over the kinematic range that has been examined, contributions have been found to be small or consistent with zero, with the most precise measurements having now pushed near to the bounds of unique interpretability. One significant limit is the precision in the knowledge of electromagnetic form factors. Presently, uncertainties in the neutron form factors  $G_E^n$  and  $G_M^n$  contribute an uncertainty to the extraction of the strange form factors of about half of the statistical error bar of the most precise  $A_{LR}$  measurements. There are important radiative corrections as well. As discussed above, the anapole moment correction in the axial term is difficult to bound with a precision approaching that of published theoretical estimates [10]. The precision of extraction of

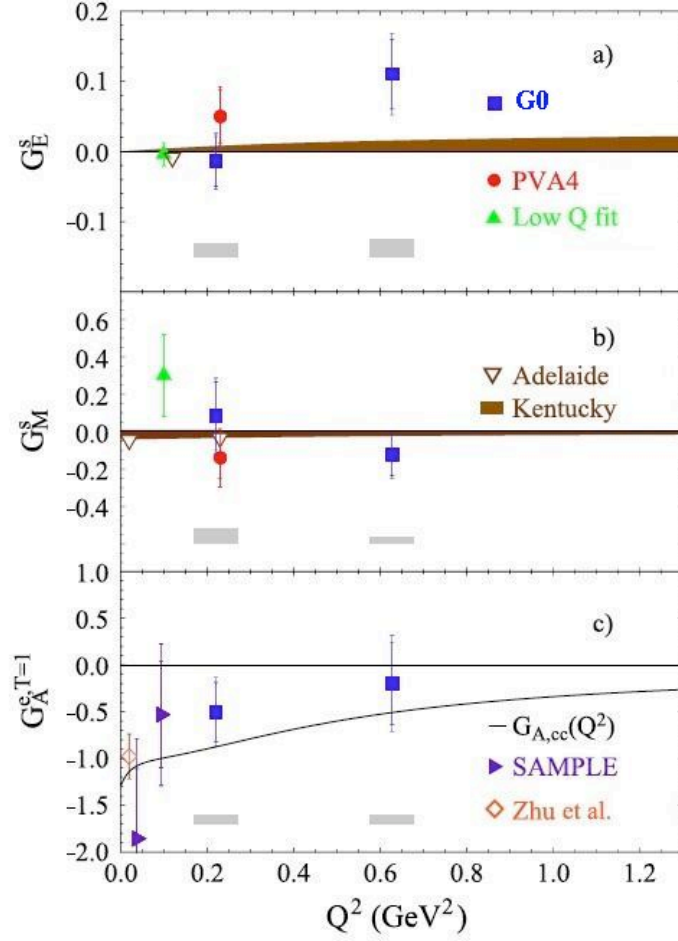


**Figure 14.** The form factors a)  $G_E^s$ , b)  $G_M^s$ , and c)  $G_A^e(T = 1)$  determined by combination of the G0 experiment forward and backward-angle measurements. Error bars show statistical and statistical plus point-to-point systematic uncertainties (added in quadrature); shaded bars below the corresponding points show global systematic uncertainties (for the G0 points). For  $G_E^s$  and  $G_M^s$ , the extraction from [46] as well as the results of the PVA4 experiment [50] are shown. Recent QCD calculations from groups at Adelaide [13, 14, 21] and Kentucky [24] are also shown; for the former the uncertainties are smaller than the symbols. For  $G_A^e(T = 1)$ , results from the SAMPLE experiment [45] are shown together with the calculation of Zhu *et al.* [10].

$G_E^s$  and  $G_M^s$  is dependent on the reliability of calculation of this correction. Similarly,  $\gamma Z$  and  $\gamma\gamma$  box diagrams present a potentially important correction to the interpretation of measurements of  $A_{LR}$ . Recent theoretical results [52, 53, 54, 55, 56] indicate that these uncertainties are sufficiently controlled for the current program, but significant advances beyond the next round of measurements would likely require further investigation into these corrections.

The extraction of the strange vector form factors also depends on the assumption of charge symmetry in the nucleon form factors. While this was once thought to provide a negligible uncertainty [17], recent work in has shown that charge symmetry violation in the nucleon may contribute to the form factor at a level comparable to the statistical error of the most precise current measurements [37, 57]. For this reason, future measurements might best be interpreted more generally, as probing all mechanisms for charge symmetry breaking in the nucleon and not

primarily the strange quark content.

As described later in this volume [25], the studies of low- $Q^2$  elastic proton electroweak scattering from the strange quark program can be combined to provide a useful constraint on parameters of the Standard Model. The Qweak experiment [58] at Jefferson Lab will take advantage of this in a future measurement of  $A_{LR}$  from proton scattering at very low  $Q^2$ , in a sensitive new search for physics beyond the Standard Model. Qweak aims for a precision which is more than an order of magnitude beyond any previous Jefferson Lab measurement. This underlines the fact that the HAPPEX and G0 experiments at Jefferson Lab have been successful not only in the measurement of strange form factors, but have forged a path for new measurements of parity-violation in electron scattering. These significant advances in production and control of polarized beam, electron beam polarimetry, high luminosity targets, low noise integration techniques, and electron beam monitoring have enabled a new generation of parity violation experiments. In this way, the legacy of the strange quark program extends to Qweak; to a very challenging measurement of the neutron radius in  $^{208}\text{Pb}$  (PREX) [59] which is so crucial in models of neutron-rich nuclei; to a measurement of parity-violation in deep inelastic scattering [60] which will improve precision on the poorly measured electroweak axial quark charges ( $C_{2q}$ ); and to the measurements (described in [25]) of electroweak couplings and valance parton distributions planned after the upcoming energy upgrade at Jefferson Lab [61, 62].

## References

- [1] R. L. Jaffe and A. Manohar, Nucl. Phys. **B337**, 509 (1990).
- [2] D. B. Kaplan and A. Manohar, Nucl. Phys. **B310**, 527 (1988).
- [3] R. D. Young, A. W. Thomas, Phys. Rev. D **81**, 014503 (2010).
- [4] S. D. Bass and A. W. Thomas, Phys. Lett. B **684**, 216 (2010).
- [5] D. H. Beck and B. R. Holstein, Int. J. Mod. Phys. E **10**, 1 (2001).
- [6] K. S. Kumar and P. A. Souder, Prog. Part. Nucl. Phys. **45**, S333 (2000).
- [7] R. L. Jaffe, Phys. Lett. B **229**, 275 (1989).
- [8] R. D. McKeown, Phys. Lett. B **219**, 140 (1989).
- [9] D. H. Beck, Phys. Rev. D **39**, 3248 (1989).
- [10] S. L. Zhu, S. J. Puglia, B. R. Holstein and M. J. Ramsey-Musolf, Phys. Rev. D **62**, 033008 (2000).
- [11] Ya. B. Zeldovich *et al.*, Zh. Eksp. Teor. Fiz. **33**, 1531 (1957) [Sov. Phys. JETP **6**, 1184 (1958)].
- [12] D. B. Leinweber, R. M. Woloshyn and T. Draper, Phys. Rev. D **43**, 1659 (1991).
- [13] D. B. Leinweber, S. Boinepalli, I. C. Cloet *et al.*, Phys. Rev. Lett. **94**, 212001 (2005).
- [14] D. B. Leinweber, S. Boinepalli, A. W. Thomas *et al.*, Phys. Rev. Lett. **97**, 022001 (2006).
- [15] D. B. Leinweber and A. W. Thomas, Phys. Rev. D **62**, 074505 (2000).
- [16] R. D. Young, D. B. Leinweber, A. W. Thomas *et al.*, Phys. Rev. D **66**, 094507 (2002).
- [17] G. A. Miller, B. M. Nefkens and I. Slaus, Phys. Rept. **194**, 1 (1990).
- [18] Particle Data Group, Phys. Rev. D **66**, 010001 (2002).
- [19] D. B. Leinweber, S. Boinepalli, A. W. Thomas *et al.*, Eur. Phys. J. A **24S2**, 79 (2005).
- [20] R. D. Young, D. B. Leinweber and A. W. Thomas, Phys. Rev. D **71**, 014001 (2005).
- [21] P. Wang, D. B. Leinweber, A. W. Thomas *et al.*, Phys. Rev. C **79**, 065202 (2009).
- [22] S. J. Dong, K. F. Liu and A. G. Williams, Phys. Rev. D **58**, 074504 (1998).
- [23] R. Lewis, W. Wilcox, R. M. Woloshyn, Phys. Rev. D **67** 013003 (2003).
- [24] T. Doi, M. Deka, S. J. Dong *et al.*, Phys. Rev. D **80**, 094503 (2009).
- [25] J. Roche, W. T. H. van Oers and R. D. Young, "Searches for Physics Beyond the Standard Model", this volume.
- [26] K. A. Aniol *et al.*, Phys. Rev. Lett. **82**, 1096 (1999).
- [27] K. A. Aniol *et al.*, Phys. Lett. B **509**, 211 (2001).
- [28] K. A. Aniol *et al.*, Phys. Rev. C **59**, 065501 (2004).
- [29] J. Alcorn *et al.*, Nucl. Instrum. Meth. A **522**, 294 (2004).
- [30] T. Nakanishi *et al.*, Phys. Lett. A **158**, 345 (1991).
- [31] T. Maruyama *et al.*, Phys. Rev. Lett. **66**, 2376 (1991).
- [32] M. Baylac *et al.*, Phys. Lett. B **539**, 8 (2002).
- [33] K. A. Aniol *et al.*, Phys. Rev. Lett. **96**, 022003 (2006).
- [34] K. A. Aniol *et al.*, Phys. Lett. B **635**, 275 (2006).
- [35] A. Acha *et al.*, Phys. Rev. Lett. **98**, 032301 (2007).

- [36] S. Ramavataram, E. Hadjimichael and T. W. Donnelly, Phys. Rev. C **50**, 1175 (1994).
- [37] M. Viviani *et al.*, Phys. Rev. Lett. **99**, 112002 (2007).
- [38] M. J. Musolf and T. W. Donnelly, Phys. Lett. B **318**, 263 (1993).
- [39] M. J. Musolf, R. Schiavilla and T. W. Donnelly, Phys. Rev. C **50**, 2173 (1994).
- [40] D. S. Armstrong *et al.*, Phys. Rev. Lett. **95**, 092001 (2005).
- [41] D. S. Armstrong *et al.*, Phys. Lett. **104**, 012001 (2010).
- [42] M. Hauger *et al.*, Nucl. Instrum. Meth. A **462**, 282 (2001).
- [43] F. E. Maas *et al.*, Phys. Rev. Lett. **93**, 022002 (2004).
- [44] F. E. Maas *et al.*, Phys. Rev. Lett. **94**, 152001 (2005).
- [45] E. J. Beise, M. L. Pitt and D. T. Spayde, Prog. Part. Nucl. Phys. **54**, 289 (2005).
- [46] J. Liu, R. D. McKeown and M. J. Ramsey-Musolf, Phys. Rev. C **76**, 025202 (2007).
- [47] R. D. Young, J. Roche, R. D. Carlini and A. W. Thomas, Phys. Rev. Lett. **97**, 102002 (2006).
- [48] J. J. Kelly, Phys. Rev. C **70**, 068202 (2004).
- [49] R. Schiavilla, J. Carlson and M. Paris, Phys. Rev. C **70**, 044007 (2004).
- [50] S. Baunack *et al.*, Phys. Rev. Lett. **102**, 151803 (2009).
- [51] “A Measurement of Nucleon Strange Form Factors at High  $Q^2$ ”, K. A. Aniol *et al.*, Jefferson Lab proposal PR-05-009 (2005).
- [52] J. A. Tjon and W. Melnitchouk, Phys. Rev. Lett. **100**, 082003 (2008).
- [53] M. Gorchtein and C. J. Horowitz, Phys. Rev. Lett. **102**, 091806 (2009).
- [54] J. A. Tjon, P. G. Blunden and W. Melnitchouk, Phys. Rev. C **79**, 055201 (2009).
- [55] H. Q. Zhou, C. W. Kao, S. N. Yang *et al.*, Phys. Rev. C **81**, 035208 (2010).
- [56] A. Sibirtsev, P. G. Blunden, W. Melnitchouk *et al.*, Phys. Rev. D **82**, 013011 (2010).
- [57] B. Kubis and R. Lewis, Phys. Rev. C **74**, 015204 (2006).
- [58] “The Qweak Experiment: A Search for New Physics at the TeV Scale Via a Measurement of the Proton’s Weak Charge”, D. Armstrong *et al.*, Jefferson Lab proposal PR-02-020 (2002).
- [59] C. J. Horowitz, S. J. Pollock, P. A. Souder and R. Michaels, Phys. Rev. C **63**, 025501 (2001).
- [60] “ $\bar{e}$ - $^2\text{H}$  Parity Violating Deep Inelastic Scattering at CEBAF 6 GeV”, X. Zheng *et al.*, Jefferson Lab proposal PR-05-007 (2005).
- [61] “An Ultra-precise Weak Mixing Angle Measurement in Møller Scattering”, K. Kumar *et al.*, Jefferson Lab proposal PR12-09-005 (2009).
- [62] “Precision Measurement of Parity-violation in Deep Inelastic Scattering Over a Broad Kinematic Range”, P. Souder *et al.*, Jefferson Lab proposal PR12-09-012 (2009).